Protocol for detection of nonsecular conversion through coherent nanooptical spectroscopy

Markus Krecik,* Sven M. Hein, Mario Schoth, and Marten Richter

Institut für Theoretische Physik, Nichtlineare Optik und Quantenelektronik, Technische Universität Berlin, Hardenbergstrasse 36, EW 7-1, 10623 Berlin, Germany

(Received 5 June 2015; published 18 November 2015)

The theoretical description of dynamics in open quantum systems becomes very demanding upon inclusion of non-Markovian effects. To simplify the computational implementation for density matrix equations of motion, the secular approximation is often applied. An experimental verification of its validity though remains difficult due to uncertainties in the system parameters and the absence of qualitatively distinct features. In this paper, we present the proposal for an experimental detection protocol sensitive to nonsecular processes neglected in the secular approximation. The protocol uses a combination of multidimensional coherent spectroscopy and nanoplasmonics. It allows for studies of nonsecular processes in various systems and provides a tool to experimentally verify the validity of the secular approximation. We apply this protocol to a system of CdSe/ZnS nanostructures and discuss the particular features originating from nonsecular processes on the resulting two-dimensional spectra.

DOI: 10.1103/PhysRevA.92.052113 PACS number(s): 03.65.Yz, 78.47.jf, 42.50.Md

I. INTRODUCTION

Open quantum systems are coupled to an external bath with many degrees of freedom, leading to dissipation of energy and potentially introducing non-Markovian effects in the system dynamics. In general, a full quantum-mechanical description of the system and its environment is unfeasible [1]. Therefore, various theoretical descriptions of time dynamics in the presence of system-bath couplings emerged, like POP (partial ordering prescription) and COP (chronological ordering prescription) [2–5], Nakajima-Zwanzig [1,6,7], time-convolutionless theory (TCL) [1,8–11], hierarchy equations [12,13], quantum kinetics [14,15], and others [16,17]. A large reduction of the computational effort is achieved through the often implicitly applied secular approximation [1,18,19]. The validity of this approximation was rarely a subject of theoretical investigations though [18,20]. In fact, it was shown that applying the secular approximation can reduce non-Markovianity [21,22], makes false or unphysical predictions [23–27], is unsuitable in description of coherence effects [28], entanglement dynamics [18,29], and breaks conservation laws [30] in special cases.

As the main result of this paper, we present a protocol for detection of nonsecular processes (i.e., processes neglected in the secular approximation) separately from secular processes. Experimental application of this protocol allows for measurement of nonsecular processes in various systems (quantum dots, biological molecules, etc.), and thus provides information about coherence transfer and non-Markovian effects.

The general idea of the protocol is the preparation of the system in a coherence $|A\rangle\langle B|$ between two different excited-state manifolds A and B (cf. Fig. 1, left). It is essential to excite these manifolds with disjoint selection rules (possible transitions with disjoint selection rules include horizontal vs vertical polarization, spin up vs spin down, magnetic vs nonmagnetic, dipole vs quadruple, etc.). Since secular processes do not convert coherences into populations (and vice versa), we will show that secular relaxation processes between these manifolds can be filtered out by a multidimensional spectroscopy setup with a measurement of populations $|A\rangle\langle A|$ and $|B\rangle\langle B|$ at the end (Fig. 1, gray box). Consequently, the measured signal contains only nonsecular processes. In this paper, we illustrate the detection of nonsecular processes between a dipole-allowed (*bright*) and quadrupole-allowed (*dark*) excited-state manifold.

To illustrate the secular approximation, we write down the equation of motion (EOM) of the density matrix $\rho(t)$ in second order Born-Markov approximation (also known as the Redfield equation) in the interaction picture:

$$\partial_t \rho_{ij}(t) = \sum_{kl} e^{i(\omega_{ij}-\omega_{kl})t} R_{ij,kl}\, \rho_{kl}(t). \tag{1}$$

Here, $R_{ij,kl}$ is the (time-independent) Redfield tensor [31,32] and $\omega_{ij} = \omega_i - \omega_j$ is the energy difference between states i and j. Providing the system is nondegenerate, the secular and nonsecular terms can be easily distinguished through their dominant time dependence. The secular approximation can be seen as a coarse-time average [27,29,33]; contributions with fast oscillating exponent can be neglected, so that only terms with $\omega_{ij} - \omega_{kl} = 0$ in Eq. (1) remain. Consequently the EOMs for populations ρ_{ii} and coherences $\rho_{ij}(i \neq j)$ decouple into

$$\begin{aligned} \partial_t \rho_{ii}(t) &= \sum_k R_{ii,kk}\, \rho_{kk}(t), \\ \partial_t \rho_{ij}(t) &= R_{ij,ij}\, \rho_{ij}(t), \end{aligned} \tag{2}$$

which gives the secular Redfield equation. The oscillating terms with nonvanishing exponent (discussed above) are the contributions from nonsecular processes. They describe transfer processes between different coherences and couplings between coherences and populations.

To detect these processes, we propose a combination between multidimensional coherent spectroscopy and nanoplasmonics. After successful application in vibrational spectroscopy [34–37], multidimensional coherent spectroscopy [38–44] advanced to a valuable tool for characterization of the electronic structure, giving access to information about, e.g., coupling between states [45–51], biexciton structure [52,53], and reconstruction of delocalized wave

*markus.krecik@tu-berlin.de

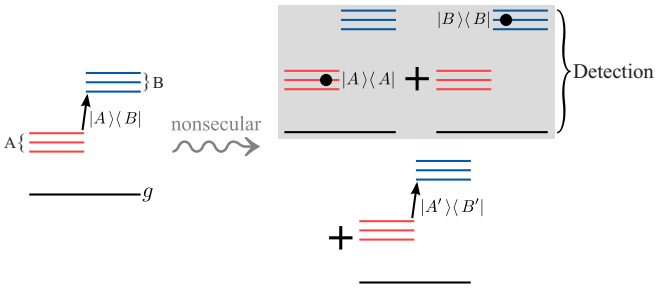

FIG. 1. (Color online) Principle of the detection protocol. Through a particular pulse sequence, the system is prepared in a coherence $|A\rangle\langle B|$ between two excited-state manifolds A and B. Only nonsecular processes are able to convert the coherences into populations $|A\rangle\langle A|$ and $|B\rangle\langle B|$ in either manifold. By only measuring the resulting populations, secular processes are filtered out. Conversion into other coherences $|A'\rangle\langle B'|$ are in principle also possible, but cannot be detected.

functions [54–56]. Its range of applications reaches from semiconductors [47,57,58] to biological complexes [45,59–66]. Recent advances in coherent multidimensional spectroscopy also allow for high spatiotemporal control [67–69].

In contrast to the more common choice of four-wave-mixing spectroscopy in combination with heterodyne detection using three exciting pulses and a local oscillator pulse [41–43], we use four phase-controlled excitation pulses with subsequent photoelectron measurement through photoemission electron microscopy (PEEM) [67]. In principle, heterodyne and fluorescence detection processes are equally possible. PEEM, however, allows for high spatial resolution and is thus advantageous for detecting single systems [67–71].

The pulse sequence used for detection is presented in Fig. 2. The color of the pulse differentiates between the addressed excited-state manifolds. Variation of the time delays τ_k between the pulses and subsequent measurement with PEEM provides a two-dimensional spectrum similar to a photon-echo signal [43].

The protocol proposed in this paper is not restricted to the simple Markovian Redfield theory depicted in Eq. (1), but is also applicable to more elaborate theoretical treatments of relaxation, like POP and COP [2–5], TCL [8–10], hierarchy equations [12,13], and other quantum kinetic equations [14,15]. For non-Markovian theories, the effects of nonsecular processes are expected to play a more significant role. Thus, the detection protocol is especially suited for

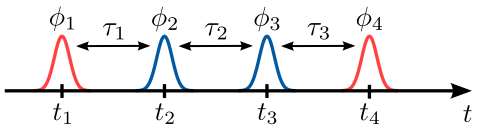

FIG. 2. (Color online) Schematic representation of the incoming laser pulses for the detection protocol. The pulses are centered around the times t_k, with time differences between the pulses $\tau_k = t_{k+1} - t_k$. For detection via phase cycling, each pulse has to have a defined phase shift ϕ_k with respect to all other pulses. The first and fourth pulse are exciting bright transitions (light red), whereas the second and third pulse are exciting dark transitions (dark blue).

investigation of nonsecular conversion processes over a broad range of nanostructures (quantum dots, biological molecules, etc.).

To open the possibility for excitation of the bright and dark state manifold we utilize nanoplasmonics, which exploits surface plasmon polaritons in metallic nanoscopic structures to generate localized electric-field enhancements [72–76]. These field enhancements may allow for increased coupling to quantum dots [77–79]. Furthermore, field gradients lead to higher-order light-matter interaction beyond the dipole approximation [80].

The second and third pulses in the pulse sequence (Fig. 2) excite dark states, whereas the other pulses excite bright states. To describe excitation of dark states, the system has to be treated by a light-matter interaction including quadrupole transitions [81]:

$$H_{e\text{-}L} = -\int d\boldsymbol{r}\, \psi^\dagger(\boldsymbol{r})\left[\boldsymbol{\mu}\cdot\boldsymbol{E}(\boldsymbol{r}_0,t) + \frac{Q}{2} : \nabla\boldsymbol{E}(\boldsymbol{r}_0,t)\right]\psi(\boldsymbol{r}). \tag{3}$$

Dipole transitions (with the dipole operator $\boldsymbol{\mu}$) are mediated through constant electric fields $\boldsymbol{E}$ in space, whereas quadrupole interactions (with the quadrupole operator Q) require an electric-field gradient $\nabla\boldsymbol{E}$. $A : B$ represents the Frobenius inner product [82], defined in Eq. (11).

In this paper, we also present a possible way of an all-optical dynamical switching between fields and field gradients through a plasmonic dolmen structure [74,83–87]. Through variation of the polarization direction of the incoming light pulse a controlled switching between the bright and dark state excitation can be achieved. The choice of the plasmonic dolmen structure becomes apparent in Sec. II C. However, other means for dynamical switching are also imaginable, like switching between electric and magnetic dipoles [88] or switching between heavy-hole and light-hole excitation [89] through structured beams.

To illustrate the method, we will apply the detection protocol to an example system and discuss the resulting spectra. Therefore we choose a spherical CdSe quantum dot (QD) embedded in a ZnS nanorod (NR) as presented in Sec. II. For demonstration purposes, we treat the relaxation by a simple Markovian Redfield model. This system is used to illustrate a possible experimental design and provides qualitative results within the right order of magnitude, though it does not have the claim for high quantitative accuracy. Readers only interested in the spectroscopic protocol can proceed to Sec. III for the general theory, and the subsequent Sec. IV for the results.

II. MODEL SYSTEM

The spectroscopic experiment is described by the Hamiltonian

$$H(t) = H_0 + H_{e\text{-}ph} + H_{e\text{-}L}(t). \tag{4}$$

The unperturbed system is described by H_0, which includes the ground state and optically excited states. The excited states form bound electron-hole pairs through Coulomb interaction: excitons and biexcitons. Between these states, relaxation occurs through exciton-phonon interaction $H_{e\text{-}ph}$. The excitation

of states through laser pulses is given by the light-matter interaction $H_{e\text{-}L}(t)$. Some of the states can be excited by dipole transitions, called bright states in the following. Contrary, dark states are forbidden by optical dipole-transition selection rules. However, the dark states considered in this paper can be excited through higher-order contributions to the light-matter interaction caused by quadrupole transitions.

A. Exciton system

For demonstration of the detection protocol, we simulate the signal caused by a single spherical CdSe QD embedded in a ZnS nanorod (NR). In systems with spherical symmetry of the electronic and phononic system, nonsecular conversion between bright and dark states does not occur due to angular momentum selection rules. Therefore, we investigate the NR system, where the symmetry is broken by cylindrical phonon modes. The QD is positioned centrally in the NR. We assume a growth direction along the y direction. The whole nanostructure is surrounded by the plasmonic dolmen structure as sketched in Fig. 4. The parameters used in the simulation are summarized in Table I.

We describe the electronic single-particle wave function of the QD under assumption of the envelope approximation [95],

$$\psi_{i,\lambda}(\boldsymbol{r}) = \varphi_{i,\lambda}(\boldsymbol{r}) u_{\lambda}^{\sigma_i}(\boldsymbol{r}), \tag{5}$$

with the band index $\lambda = \{v,c\}$, the energy level i, spin index $\sigma_i = \{+,-\}$, the envelope wave function $\varphi_{i,\lambda}(\boldsymbol{r})$, and the Bloch wave function $u_{\lambda}^{\sigma_i}(\boldsymbol{r})$ for wave vectors $\boldsymbol{k} = 0$. For calculating $\varphi_{i,\lambda}(\boldsymbol{r})$, we treat the QD as a spherical potential well with finite barriers and radius R. The depth of the confinement potential is determined by the valence-band offset V_v, conduction-band offset V_c, and band gap ε_g between CdSe and the surrounding ZnS [91,93].

A single optical excitation creates an electron-hole pair in the QD, forming an exciton through Coulomb interaction.

TABLE I. Computational parameters for CdSe and ZnS. The excitonic wave functions in the CdSe QD of radius R were computed with help of the effective masses of electrons m_e^* and holes m_h^*, band gap ε_g, and valence- and conduction-band offset V_v and V_c. For the exciton-phonon interaction using the expressions from [90], the effective masses m_e^* and m_h^* of ZnS, the dielectric constant ε_0 and ε_∞, energy of transverse optical phonons ω_{TO}, lattice constants a and c were used. R and d are radius and length of the NR.

CdSe	ZnS
$m_e^* = 0.12 m_e$[a]	$m_e^* = 0.27 m_e$[a]
$m_h^* = -0.9 m_e$[a]	$m_h^* = -1.4 m_e$[a]
$\varepsilon_g = 1.75$ eV[a]	$\epsilon_0 = 8.3$[b]
$V_v = -0.6$ eV[c]	$\epsilon_\infty = 5.2$[b]
$V_c = 1.39$ eV[c]	$\omega_{\mathrm{TO}} = 34$ meV[d]
$R = 3.0$ nm	$a = 0.38$ nm[a]
	$c = 0.62$ nm[a]
	$R = 4.0$ nm
	$d = 20$ nm

[a]Reference [91].
[b]Reference [92].
[c]Reference [93].
[d]Reference [94].

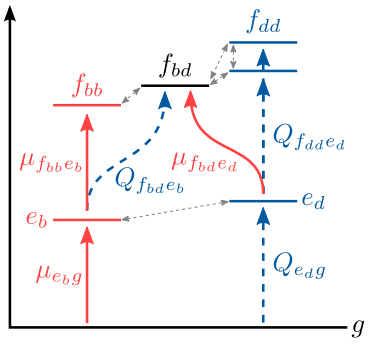

FIG. 3. (Color online) Level scheme of the lowest excitonic and biexcitonic states. Solid arrows indicate dipole-allowed transitions and dashed arrows dipole-forbidden transitions. The relevant optical transition elements for each excitation are labeled accordingly. The small dashed arrows indicate possible conversion processes.

Double excitations lead to the formation of biexcitons with slightly shifted binding energies. The Hamiltonian for the system consists of an electronic and phononic part, respectively:

$$H_0 = \sum_m \varepsilon_m |m\rangle\langle m| + \sum_q \hbar\omega_q b_q^\dagger b_q. \tag{6}$$

Its derivation and the definition of the excited states $|m\rangle$ are given in Appendix A. The phononic part of H_0 describes optical vibrational modes of the NR with energy ω_q, with bosonic creation and annihilation operators $b_q^\dagger, b_q$. The energy of the ground state $|g\rangle$ is chosen to be zero. The exciton energies ε_m are obtained from the Hamiltonian of the envelope wave function within the effective-mass approximation including Coulomb shifts.

For the simulation, we considered only the lowest excitonic and biexcitonic levels, as shown in the level scheme, Fig. 3. The excitonic manifold consists of a bright state $|e_b\rangle$ with an electron in the 1_s state and a heavy hole in the 1_s state. The three degenerate dark excitons $|e_d\rangle$ are in a 1_s-electron and 1_p-hole state. All excitonic states have an additional twofold spin degeneracy. The biexcitonic manifold is constructed from these excitonic states. It includes one bright state $|f_{bb}\rangle$, nine dark states $|f_{dd}\rangle$, and six mixed states $|f_{bd}\rangle$.

B. Exciton-light interaction

The crucial part of the proposed detection protocol is a controlled switching between bright state excitations [via dipole matrix element $\boldsymbol{\mu}$ in Eq. (3)] and dark state excitations (via quadrupole matrix element Q) in the QD.

The usual assumption for describing light interaction with QDs is a spatially constant electric field since its wavelength is much larger than the nanostructure. Electric-field gradients and thus quadrupole excitations are negligible [96]. This is incorporated in the dipole approximation, where only dipole transitions are considered in the description of semiclassical exciton-light interaction.

In Sec. II C, we present the plasmonic dolmen structure, which can create localized field gradients and enables us to achieve a switching between bright and dark state excitations. To describe the interaction with the QD for this case, we

have to extend the interaction Hamiltonian beyond the dipole approximation. Therefore, we consider the semiclassical light-matter interaction given in Eq. (3) where the full electric field $\boldsymbol{E}(\boldsymbol{r},t)$ is already expanded up to first order to account for dipole and the quadrupole transitions, respectively [81]. The dipole operator is given by $\boldsymbol{\mu} = e\,\boldsymbol{r}$ and the quadrupole operator $Q = e\,\boldsymbol{r}\circ\boldsymbol{r}$. Here, $\boldsymbol{a}\circ\boldsymbol{b} = (a_i b_j)$ denotes the dyadic product.

The detection protocol uses four ultrashort light pulses as depicted in Fig. 2. Therefore, we split the electric field into four nonoverlapping pulses, which we factorize into its spatial and temporal part:

$$\begin{aligned}\boldsymbol{E}(\boldsymbol{r}_0,t) &= \sum_{k=1}^{4} \boldsymbol{E}_{\boldsymbol{r}}^{\nu_k}(\boldsymbol{r}_0) E_t^k(t-t_k),\\ E_t^k(t-t_k) &= \tilde{E}_k(t-t_k)e^{-i\omega_k(t-t_k)+i\phi_k}\\ &\quad + \tilde{E}_k^*(t-t_k)e^{+i\omega_k(t-t_k)-i\phi_k},\end{aligned} \tag{7}$$

with envelopes $\tilde{E}_k(t-t_k)$ centered at time t_k. The spatial component $\boldsymbol{E}_{\boldsymbol{r}}^{\nu_k}(\boldsymbol{r}_0)$ is calculated in a scattering simulation of the plasmonic dolmen structure for cw excitation (see Sec. II C). This factorization is valid as long as the field distribution is largely independent of the excitation frequency within the pulse bandwidth.

We assume that each pulse interacts with frequency ω_k resonantly with the system, and has a defined phase shift ϕ_k with respect to the other pulses. The index k labels the pulses and $\nu_k = \{x,y\}$ their polarization direction. In Appendix B, we apply the envelope approximation, to obtain the light-matter interaction Hamiltonian

$$H_{e\text{-}L} = -\sum_{k=1}^{4} \sum_{\substack{mn\\ \text{interband}}} \tilde{\mathcal{M}}_{mn}^{\nu_k} E_t^k(t-t_k)|m\rangle\langle n|, \tag{8}$$

where we introduced the coupling

$$\tilde{\mathcal{M}}_{mn}^{\nu_k} = \boldsymbol{\mu}_{mn}\cdot\boldsymbol{E}_{\boldsymbol{r}}^{\nu_k}(\boldsymbol{r}_0) + Q_{mn} : \nabla^S \boldsymbol{E}_{\boldsymbol{r}}^{\nu_k}(\boldsymbol{r}_0). \tag{9}$$

Here, $\nabla^S \boldsymbol{E} = 1/2(\nabla\boldsymbol{E} + \nabla\boldsymbol{E}^T)$ is the symmetrized tensor of the field gradient. The considered field coupling elements $\tilde{\mathcal{M}}_{mn}^{\nu_k}$ only induce interband transitions, thus $\tilde{\mathcal{M}}_{e_m e_n}^{\nu_k} = \tilde{\mathcal{M}}_{f_m f_n}^{\nu_k} = 0$. Direct excitation from the ground state to the biexciton manifold is also forbidden, $\tilde{\mathcal{M}}_{f_m g}^{\nu_k} = 0$, since each light interaction only creates one electron-hole pair. The coupling for biexcitons $|f_{ij}\rangle$ consisting of the excitons $|e_i\rangle$ and $|e_j\rangle$ is defined over the excitonic coupling elements $\tilde{\mathcal{M}}_{f_{ij}e_k}^{\nu_k} = \delta_{ki}\tilde{\mathcal{M}}_{e_j g}^{\nu_k} + \delta_{kj}\tilde{\mathcal{M}}_{e_i g}^{\nu_k}$.

In the following, we focus on the excitonic coupling elements, given through

$$\begin{aligned}\boldsymbol{\mu}_{e_m g} &= e\,S_{e_m g}\boldsymbol{d}_{cv}^{\sigma_{e_m}},\\ Q_{e_m g} &= e\,\boldsymbol{d}_{cv}^{\sigma_{e_m}}\circ\boldsymbol{m}_{e_m g}.\end{aligned} \tag{10}$$

e is the electron charge. The Frobenius inner product is defined as [82]

$$A : B = \sum_{ij} A_{ij}B_{ij}. \tag{11}$$

The microscopic dipole element $\boldsymbol{d}_{cv}^{\sigma_{e_m}}$ is given through

$$\boldsymbol{d}_{cv}^{\sigma_{e_m}} = \boldsymbol{d}_{vc}^{\sigma_{e_m}*} = \int_{UC} d\boldsymbol{r}'\, u_c^{\sigma_{e_m}*}(\boldsymbol{r}')\,\boldsymbol{r}'\,u_v^{\sigma_{e_m}}(\boldsymbol{r}')\delta_{\sigma_{e_m}\sigma_{e_n}}. \tag{12}$$

The overlap $S_{e_m g}$ and dipole matrix element $\boldsymbol{m}_{e_m g}$ of the electron and hole envelope wave functions $\varphi_{e_m,c}(\boldsymbol{r})$ and $\varphi_{e_m,v}(\boldsymbol{r})$ are respectively

$$\begin{aligned}S_{e_m g} &= S_{g e_m}^* = \int d\boldsymbol{r}\,\varphi_{e_m,c}^*(\boldsymbol{r})\varphi_{e_m,v}(\boldsymbol{r}),\\ \boldsymbol{m}_{e_m g} &= \boldsymbol{m}_{g e_m}^* = \int d\boldsymbol{r}\,\varphi_{e_m,c}^*(\boldsymbol{r})\boldsymbol{r}\varphi_{e_m,v}(\boldsymbol{r}).\end{aligned} \tag{13}$$

Since the envelope wave functions $\varphi_{m,\lambda}(\boldsymbol{r})$ have a set parity, we get opposite selection rules for S_{mn} (no parity change) and $\boldsymbol{m}_{mn}$ (parity change). As a consequence, $\boldsymbol{\mu}_{mn}$ and Q_{mn} have disjoint subsets of allowed transitions. $\boldsymbol{\mu}_{mn}$ leads to dipole-allowed bright transitions, indicated by the solid red line in the level scheme Fig. 3. Q_{mn} acts on the other subset of dipole-forbidden dark transitions, denoted by dashed blue lines.

C. Plasmonic dolmen

In the preceding section, we presented the foundation for nanostructures interacting with electric-field gradients. However the question remains how to create such field distributions. Plasmonic structures are generally known to create strong electric fields and field gradients [97–99], and are good candidates for excitation of quadrupole transitions. For our objective though, two additional requirements on the plasmonic structure are necessary. First, dipole and quadrupole transitions have to be excited selectively, meaning, a dipolar excitation has to have a negligible quadrupole contribution and vice versa. And second, there has to be a simple way of switching dynamically between both types of excitation.

For plasmonic structures with high symmetry, a selective switching between fields and field gradients cannot be accomplished. We demonstrate the feasibility of the protocol for bright and dark state excitation using a plasmonic structure known from the literature as plasmonic dolmen [74,83–87], which is often studied in the context of Fano resonances [83,100]. However, other plasmonic structures, like plasmonic trimers [101], might be equally suitable for the protocol. As depicted in Fig. 4, the dolmen structure consists of a single bar, which supports dipolar plasmonic modes. Perpendicular to it are two parallel bars supporting nonradiative quadrupolar plasmonic modes. A y-polarized light pulse incoming perpendicular to the dolmen structure (along the z axis; compare Fig. 4) couples to the parallel bars, thus exciting dipolar plasmonic modes. Light polarized along the x axis will excite a dipolar mode in the single bar, which couples into the parallel bars and excites quadrupolar plasmon modes. (It should be noted that dipolar and quadrupolar plasmonic modes should not be confused with the dipole and quadrupole excitations in the QD mediated by fields or field gradients at the position of the QD.)

As the discussion in this section will show, through careful placement within the plasmonic dolmen structure, a nanostructure or molecule experiences predominantly dipole or quadrupole excitations, which can be switched through the polarization of the incoming light pulse.

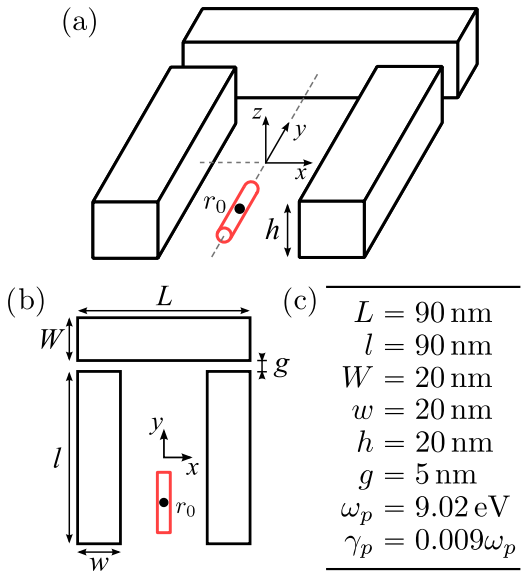

FIG. 4. (Color online) Sketch of the plasmonic dolmen structure (a) in three dimensions with the placement and direction of the QD/NR indicated in light red at $\boldsymbol{r}_0$. (b) Top view with all relevant dimensions. The coordinate system is centered in the middle of the structure. The dimensions of the dolmen structure and material parameters (corresponding to gold [84]) used in the simulations are shown in (c).

For a small thickness h of the plasmonic structure, retardation effects can be neglected. Due to the symmetry of the structure, suitable points for switching between bright and dark state excitation are expected to be along the y axis centered in the structure $x = z = 0$.

The strength of the light-matter coupling in the QD depends on the overlap S_{mn} and dipole elements $\boldsymbol{m}_{mn}$ of the envelope wave functions, Eq. (13), and through the microscopic dipole element $\boldsymbol{d}_{cv}^{\sigma_m}$ [Eq. (12)] also on the lattice orientation. We assume a lattice growth direction of the QD along the y axis, so that the microscopic dipole element is $\boldsymbol{d}_{cv}^{\pm} = 1/\sqrt{2}(1,0,\pm i)$ for spin-up and spin-down states, respectively [102,103].

To analyze the switching properties of the dolmen structure, we performed FEM simulations [104] of steady-state scattering under cw excitation. With the obtained scattered field amplitudes and gradients, we computed the corresponding dipole-field coupling $\boldsymbol{\mu}_{e_b g} \cdot \boldsymbol{E}_{\boldsymbol{r}}^{\nu_k}$ and quadrupole-field coupling $Q_{e_d g} : \nabla^S \boldsymbol{E}_{\boldsymbol{r}}^{\nu_k}$ across the structure. In the following, we will compare the absolute value of both field couplings for both polarization directions $\nu_k = \{x,y\}$ of the incoming light pulse. We look at the excitation of spin-up states exemplarily, thus $\boldsymbol{d}_{cv}^{+} = 1/\sqrt{2}(1,0,+i)$. The distribution of dipole-field and quadrupole-field coupling in the $y-z$ plane in the middle of the structure ($x = 0$) is depicted in Figs. 5(a)–5(d). The laser energy of 2.0 eV used in the simulation corresponds to the QD transition energy. In Figs. 5(a) and 5(b), the dipole-field couplings $|\boldsymbol{\mu}_{e_b g} \cdot \boldsymbol{E}_{\boldsymbol{r}}^{x}|$ and $|\boldsymbol{\mu}_{e_b g} \cdot \boldsymbol{E}_{\boldsymbol{r}}^{y}|$ are compared. One can see an efficient excitation of spin-up states around $\boldsymbol{r}_0 = (0,-38\,\mathrm{nm},0)$ for x-polarized light [Fig. 5(a)]. Upon changing the polarization to a y-polarized beam, the dipole-field coupling vanishes altogether along the y axis (b).

The comparison of the quadrupole-field couplings across the structure shows the opposite picture. $|Q_{e_d g} : \nabla^S \boldsymbol{E}_{\boldsymbol{r}}^{x}|$ [Fig. 5(c)] has a negligible contribution at $\boldsymbol{r}_0$, whereas for y polarization, $|Q_{e_d g} : \nabla^S \boldsymbol{E}_{\boldsymbol{r}}^{y}|$ [Fig. 5(d)] has its highest contribution. From this behavior of the dipole-field and quadrupole-field couplings, we conclude an effective switching between bright and dark state excitation for a QD placed at $\boldsymbol{r}_0$. The position and size of the QD at $\boldsymbol{r}_0$ is displayed as a gray dot. The switching is mediated through changing the polarization of the incoming light pulse between $\nu_k = x$ (dipole excitation) and $\nu_k = y$ (quadrupole excitation).

As a consequence for the coherent spectroscopy setup, the electric field for reproducing the pulse sequence from Fig. 2 with Eq. (7) becomes

$$\boldsymbol{E}(\boldsymbol{r}_0,t) = \boldsymbol{E}_{\boldsymbol{r}}^{x}(\boldsymbol{r}_0)E_t^1(t-t_1) + \boldsymbol{E}_{\boldsymbol{r}}^{y}(\boldsymbol{r}_0)E_t^2(t-t_2) + \boldsymbol{E}_{\boldsymbol{r}}^{y}(\boldsymbol{r}_0)E_t^3(t-t_3) + \boldsymbol{E}_{\boldsymbol{r}}^{x}(\boldsymbol{r}_0)E_t^4(t-t_4). \quad (14)$$

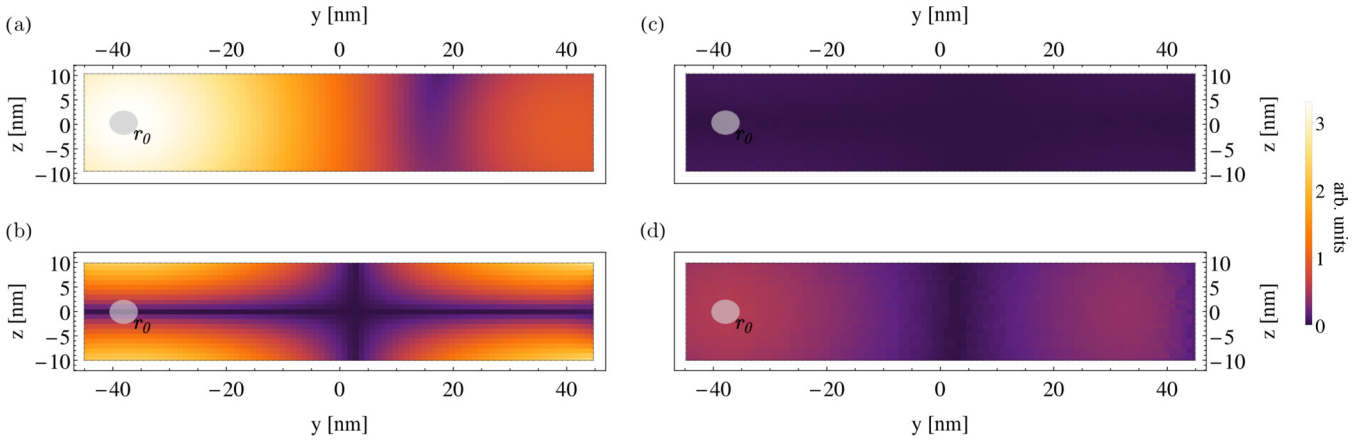

FIG. 5. (Color online) Left side: Comparison between (a) $|\boldsymbol{\mu}_{e_b g} \cdot \boldsymbol{E}_{\boldsymbol{r}}^{x}|$ and (b) $|\boldsymbol{\mu}_{e_b g} \cdot \boldsymbol{E}_{\boldsymbol{r}}^{y}|$ in the $y-z$ plane of the dolmen structure. Right side: Comparison between (c) $|Q_{e_d g} : \nabla^S \boldsymbol{E}_{\boldsymbol{r}}^{x}|$ and (d) $|Q_{e_d g} : \nabla^S \boldsymbol{E}_{\boldsymbol{r}}^{y}|$ in the $y-z$ plane. The microscopic dipole matrix element $\boldsymbol{d}_{cv}^{+}$ corresponds to spin-up excitation. An enhancement of dipole transitions for x-polarized light (a) can be seen around $\boldsymbol{r}_0 = (0,-38\,\mathrm{nm},0)$, which gets suppressed upon excitation with y-polarized light (b). Whereas the quadrupole excitation is negligible for x-polarized light (c), an enhancement of quadrupole excitations is visible around $\boldsymbol{r}_0$ in y polarization (d). The position and size of the QD at $\boldsymbol{r}_0$ is marked as a gray dot.

We define a switching quality of the plasmonic structure, obtained from the field-coupling values in $\boldsymbol{r}_0$ extracted from the simulation:

$$\eta_x = \frac{\left|\boldsymbol{\mu}_{e_b g} \cdot \boldsymbol{E}^x_{\boldsymbol{r}}\right|}{\left|Q_{e_d g} : \boldsymbol{\nabla}^S \boldsymbol{E}^x_{\boldsymbol{r}}\right|} = 530, \qquad \eta_y^{-1} = \frac{\left|Q_{e_d g} : \boldsymbol{\nabla}^S \boldsymbol{E}^y_{\boldsymbol{r}}\right|}{\left|\boldsymbol{\mu}_{e_b g} \cdot \boldsymbol{E}^y_{\boldsymbol{r}}\right|} = 39. \tag{15}$$

η_x indicates quadrupole transition suppression compared to dipole transitions for x-polarized light. η_y^{-1} expresses the suppression of dipole transitions for y-polarized light. An analysis of the plasmonic dolmen structure for spin-down excitation, $\boldsymbol{d}^-_{cv} = 1/\sqrt{2}(1,0,-i)$, would show a similar picture for the switching point $\boldsymbol{r}_0$ and the switching quality η_{ν_k}.

As will be discussed in Sec. IV, the better the switching quality, the better is the detection of nonsecular processes. For $\eta_x = \eta_y^{-1} = \infty$ (i.e., $Q_{mn} : \boldsymbol{\nabla}^S \boldsymbol{E}^x_{\boldsymbol{r}} = \boldsymbol{\mu}_{mn} \cdot \boldsymbol{E}^y_{\boldsymbol{r}} = 0$), it becomes perfect. This is in realistic cases not feasible. The switching quality may get modified through the spatial extent of the wave function in the QD. In our setup, the electronic wave function is mostly centered in the QD, so that the effective radius of interaction is smaller than the QD depicted in Fig. 5. In the case of larger nanostructures, a weighted average over the electric-field distribution with the excitonic wave function has to be performed, which must be taken into consideration for experimental application.

Magnetic dipole interactions have a negligible influence on the switching properties of the dolmen structure in $\boldsymbol{r}_0$ (calculation not included in the paper). For x-polarized light, they introduce an error comparable to the negligible electric quadrupole contribution, whereas for y-polarized light, the magnetic dipole interaction is about as strong as the (suppressed) electric dipole interaction and thus not relevant. Therefore, magnetic dipole interactions introduce only an additional minor error in the resulting spectra.

D. Exciton-phonon relaxation

For demonstration of the detection protocol, we consider the most simple relaxation theory of exciton-phonon interaction in the model system. Therefore, we derive the relaxation Green function in Born-Markov approximation in the following.

We take into account an exciton-phonon interaction Hamiltonian nondiagonal in the excitonic states:

$$H_{e\text{-}ph} = \hbar \sum_{\substack{mn \\ \text{intraband}}} \sum_q \left(g_q^{mn} b_q^\dagger + g_q^{nm*} b_q\right) |m\rangle\langle n|. \tag{16}$$

The detailed microscopic derivation and the form of the exciton-phonon coupling element g_q^{mn} is given in Appendix C. The phonon energies are too small to induce interband transitions, so it is sufficient to include in the sum only intraband combinations of states like $|e_m\rangle\langle e_n|$ and $|f_m\rangle\langle f_n|$. The ground state is not affected by phonon relaxation. We only consider optical-phonon modes for the cylindrical ZnS NR, since acoustic modes do not have enough energy to bridge the energy difference between the excited states. The modes were computed under the assumption that the perturbation by the CdSe QD within the NR is negligible. The multi-index q in the sum accounts for all quantum numbers of longitudinal optical ($q = \{n,l,m\}$) and side-surface optical ($q = \{n,m\}$) phonons [90].

To obtain the relaxation Green function $\mathcal{G}(t)$, we solve the von-Neumann equation for the phonon-coupling Hamiltonian, Eq. (16), in the interaction picture:

$$\partial_t \rho(t) = -\frac{i}{\hbar}[H_{e\text{-}ph}(t), \rho(t)] = \mathcal{L}_{e\text{-}ph}(t)\rho(t). \tag{17}$$

We introduced the Liouvillian (or superoperator) through $\mathcal{L}_{e\text{-}ph}\rho = -i/\hbar[H_{e\text{-}ph}, \rho]$. The EOM for the density matrix elements $\rho_{ij}(t) = \langle i|\rho(t)|j\rangle$ in Born-Markov approximation becomes

$$\partial_t \rho_{ij}(t) = \int_0^\infty d\tau \, \mathrm{tr}\{(\mathcal{L}_{e\text{-}ph}(t-\tau)\mathcal{L}_{e\text{-}ph}(t)|j\rangle\langle i|)\rho_{\mathrm{tot}}(t)\}. \tag{18}$$

The trace involves a summation over system and bath degrees of freedom, which we evaluate in the bath approximation $\rho_{\mathrm{tot}}(t) = \rho(t) \otimes \rho_B$. The expectation values of bath variables are $\langle b_p^\dagger b_q \rangle_B = \mathrm{tr}_B\{b_p^\dagger b_q \rho_B\} = \delta_{pq} n(\omega_q)$ with the Bose distribution $n(\omega) = (e^{\hbar\omega/(k_B T)} - 1)^{-1}$, which we evaluate at $T = 80$ K. Thus, we obtain the Redfield equation

$$\begin{aligned} \partial_t \rho_{ij} &= \sum_{kl} e^{i\omega_{il}t} R^{ik}_{kl} \rho_{lj} + e^{i\omega_{lj}t} R^{jk*}_{kl} \rho_{il} \\ &\quad - e^{i(\omega_{ik}+\omega_{lj})t}\left(R^{lj}_{ik} + R^{ki*}_{jl}\right)\rho_{kl}, \\ \partial_t \rho_{ig} &= \sum_{kl} e^{i\omega_{il}t} R^{ik}_{kl} \rho_{lg} \end{aligned} \tag{19}$$

with

$$\begin{aligned} R^{ij}_{kl} &= -\pi\left(J^{ij}_{kl}(\omega_{kl}) n(\omega_{kl}) \theta(\omega_{kl}) + J^{kl}_{ij}(\omega_{lk})(1+n(\omega_{lk}))\theta(\omega_{lk})\right) \\ &\quad + \gamma^{pd}_{ij} \delta_{ik}\delta_{jl}(1-\delta_{ij}). \end{aligned} \tag{20}$$

In above expression, we introduced the spectral density $J^{ij}_{kl}(\omega) = \sum_q g^{ij}_q g^{lk*}_q \delta(\omega - \omega_q)$. We included pure-dephasing processes between interband coherences through $\gamma^{pd}_{ij} \equiv \gamma^{pd}_{ji}$. For $T = 80$ K, it is given by $\hbar\gamma^{pd}_{eg} = \hbar\gamma^{pd}_{fe} = 5$ meV, $\gamma^{pd}_{fg} = 2\gamma^{pd}_{eg}$ [105] for the respective excitonic and biexcitonic manifolds e and f. The relaxation Green function $\mathcal{G}(t,t_0)$ is the solution to Eq. (19) through $\rho(t) = \mathcal{G}(t,t_0)\rho(t_0)$.

Secular approximation

We now apply the secular approximation to Eq. (19). Through this approximation, the involved relaxation time scales are well reproduced, though some non-Markovian and coherence effects may disappear [18]. As was already discussed in the Introduction, the EOM of the density matrix (19) is decomposed into oscillating and nonoscillating terms. The former ones will eventually average out. Therefore only nonoscillating, resonant terms are kept in the secular approximation:

$$\begin{aligned} \partial_t \rho_{ij} &= \left[\sum_k \left(R^{ik}_{ki} + R^{jk*}_{kj}\right) - \left(R^{jj}_{ii} + R^{ii*}_{jj}\right)\right]\rho_{ij} \\ &\quad - \delta_{ij} \sum_{k(\neq i)} \left(R^{ki}_{ik} + R^{ki*}_{ik}\right)\rho_{kk}, \\ \partial_t \rho_{ig} &= \sum_k R^{ik}_{ki} \rho_{ig}. \end{aligned} \tag{21}$$

As a result, the EOM for populations $i = j$ decouple from the coherences $i \neq j$, simplifying the computational effort considerably.

The construction of the secular Redfield equation, Eq. (21), is only valid for nondegenerate systems [106]. Nevertheless we can apply it to our degenerate model system since we are only interested in the detection of nonsecular conversion *between* the bright and dark state manifolds. These two sets of states are not degenerate so that the form of Eq. (21) holds. An application considering nonoscillating terms within each manifold would introduce additional nonsecular processes only within the respective manifold, possibly leading to faster dephasing and a weaker signal. As was verified in additional simulations, including these terms in our model has a negligible impact on the final spectra. Therefore, the discussion of the results in secular approximation takes place using Eq. (21).

III. DETECTION METHOD

In this section, we present the detection protocol for nonsecular conversion processes. The protocol consists of four incoming light pulses, interacting with the system; and subsequent detection through photoemission of an electron. Similar to polarization-selective 2D spectroscopy [47], we vary the polarization of the incoming light pulses. The polarization of the first and fourth pulses is $\nu_1 = \nu_4 = x$, leading to excitation of bright states. The second and third pulses excite dark states through a y-polarized beam, $\nu_2 = \nu_3 = y$ [cf. Eq. (14) and Fig. 2]. The special choice of the polarization directions prevents the system from forming excited-state populations, ultimately resulting in the suppression of secular processes. Similar detection protocols involving heterodyne or fluorescence detection can be formulated in a similar way.

In the following, we will derive the signal created by the detection protocol. Therefore, we formulate the protocol in a general fashion, so that it is independent of the specific system and Green function. Instead of bright and dark state manifolds, it can also be applied to other properties of nanostructures, which are independently optically excitable (e.g., study of coherence transfer in spin-flip processes with spin-up and spin-down excitation through left and right circularly polarized light). This leaves a broad range of applications for this detection protocol of nonsecular conversion processes.

We consider a measurement through PEEM [67–71]. After interaction with the fourth pulse, the excited electron (population) will be ionized through an additional high-energy pulse. Through knowledge of the ionization energy, one obtains the kinetic energy of the electron and can deduce the excited-state energies. We will not include the photoionization process of PEEM in our discussion, but rather focus on evaluating the electron density within a small ionization energy window. We set this window around the excited-state manifolds. We start with the time evolution of the density matrix $\rho(t)$. In the interaction picture with respect to H_0, the system is driven by the exciton-phonon and exciton-light interaction:

$$\begin{aligned}\partial_t \rho(t) &= -\frac{i}{\hbar}[H_{e\text{-}ph}(t) + H_{e\text{-}L}(t), \rho(t)] \\ &= [\mathcal{L}_{e\text{-}ph}(t) + \mathcal{L}_{e\text{-}L}(t)]\rho(t). \end{aligned} \tag{22}$$

The general solution to above equation is given as the propagator $U(t,t_0)$ through

$$\rho(t) = U(t,t_0)\rho(t_0). \tag{23}$$

Using the Feynman disentanglement theorem [107], we separate the phonon interaction from the light interaction:

$$U(t,t_0) = \mathcal{G}(t,t_0) T \exp\left(\int_{t_0}^{t} dt'\, \mathcal{G}(t_0,t')\mathcal{L}_{e-L}(t')\mathcal{G}(t',t_0)\right), \tag{24}$$

so that we are able to treat the electric field in perturbation theory with respect to $\mathcal{L}_{e\text{-}L}$ for arbitrary Green functions $\mathcal{G}(t,t_0)$. The propagator $\mathcal{G}(t,t_0)$ was already computed in the previous section for the model system within the Redfield theory. Since $H_{e\text{-}ph}$ is not explicitly time dependent, we can replace in the following $\mathcal{G}(t'_{j+1},t'_j) \to \mathcal{G}(\tau'_j)$, using the time differences $\tau'_j = t'_{j+1} - t'_j$. T denotes the chronological time-ordering operator.

The pulse sequence, Eq. (7), consists of four ultrashort pulses as is shown in Fig. 2. We assume the system to be excited resonantly by the light pulses, thus the application of the rotating wave approximation (RWA) is justified. Consequently, each quantum pathway can be identified through a defined phase dependence $\phi = \pm\phi_1 \pm \phi_2 \pm \phi_3 \pm \phi_4$ [108]. Through phase cycling, the signal can be filtered for a single phase combination and thus for particular quantum pathways. Therefore, the experiment will be repeated for different phase combinations. Through linear combination, specific pathways and thus specific spectroscopic signals are selected [40,43]. We use the phase combination of the photon-echo signal $\phi_s = -\phi_1 + \phi_2 + \phi_3 - \phi_4$ [40].

The first occurrence of this particular phase combination in the Dyson series of the propagator (24) is in the fourth-order expansion in the electric field:

$$\begin{aligned}\rho^{(4)}(t) = &\int_{t_0}^{t} dt'_4\, \mathcal{G}(\tau'_4)\mathcal{L}_{e\text{-}L}(t'_4) \int_{t_0}^{t'_4} dt'_3\, \mathcal{G}(\tau'_3)\mathcal{L}_{e-L}(t'_3) \\ &\times \int_{t_0}^{t'_3} dt'_2\, \mathcal{G}(\tau'_2)\mathcal{L}_{e\text{-}L}(t'_2) \int_{t_0}^{t'_2} dt'_1\, \mathcal{G}(\tau'_1)\mathcal{L}_{e\text{-}L}(t'_1)\rho_0(t'_1). \end{aligned} \tag{25}$$

To evaluate the density matrix elements $\rho^{(4)}_{ij}(t) = \langle i|\rho^{(4)}(t)|j\rangle$, we note that the action of the relaxation Green function $\mathcal{G}(\tau)$ in Hilbert space is

$$\mathcal{G}(\tau)|k\rangle\langle l| = \sum_{ij} |i\rangle\langle j|\mathcal{G}_{ij,kl}(\tau). \tag{26}$$

The pulses are short compared to the relaxation times, so we can replace the time argument in $\mathcal{G}(\tau'_j)$ by the pulse delay times: $\mathcal{G}(\tau'_j) \to \mathcal{G}(\tau_j)$. With Eq. (8) and the RWA, we can evaluate the Liouvillians $\mathcal{L}_{e-L}$ in Eq. (25). Each resulting term is called Liouville pathway and can be written as a double-sided Feynman diagram [43].

The detected PEEM signal is proportional to the total electron density within an ionization energy window, which is given by the sum over the diagonal elements of the system density matrix:

$$n_e = \sum_m \rho_{e_m e_m} + 2\sum_m \rho_{f_m f_m}. \tag{27}$$

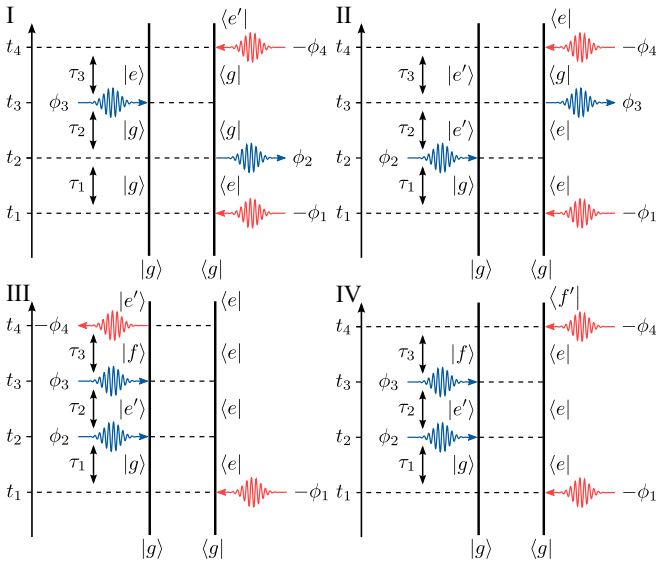

FIG. 6. (Color online) Double-sided Feynman diagrams for the remaining Liouville pathways in the PEEM measurement with the phase-cycling condition $\phi_s = -\phi_1 + \phi_2 + \phi_3 - \phi_4$. The photon-ionization process is not depicted. The diagrams correspond to (I) GSB, (II) ESE, (III) and (IV) ESA. Coloring of the light pulses corresponds to bright (light red) and dark (dark blue) state excitation.

This expression is only valid for undoped semiconductor systems, where the excitonic state $|e_m\rangle$ consists of one electron-hole pair and the biexcitonic state $|f_m\rangle$ of two electron-hole pairs (hence the factor 2 in the second term). For systems with different carrier numbers in exciton and biexciton states, as in molecules or doped semiconductors, Eq. (27) has to be modified by the actual number of electrons present in states within ionization energy range.

Besides being able to detect signals with high spatial resolution, the photoelectron measurement with PEEM has the advantage that the ground state ρ_{gg} will not be probed. This reduces the actual number of contributing pathways in the signal [Eq. (27)] to 4, in contrast to other four-pulse methods. Their corresponding Feynman diagrams are depicted in Fig. 6.

Diagram I in Fig. 6 corresponds to the ground-state bleaching process (GSB), describing the formation of a depopulated ground state after the first pulse. The second diagram in Fig. 6 depicts the excited-state emission process (ESE), inducing a stimulated emission of the excited state through the third pulse. The remaining two pathways III and IV constitute excited-state absorption processes (ESA), where the third interaction leads to further absorption and formation of biexcitons. The fourth pathway interferes destructively with all other pathways due to an overall opposite sign. The respective analytic expressions for the diagrams are given in Appendix D.

The Fourier transformed electric pulses are given through $\tilde{E}_k(\omega_k) = \int dt\, \tilde{E}_k(t) e^{-i\omega_k t}$. To achieve the excitation of bright and dark states corresponding to the pulse sequence in Fig. 2, the polarization of the pulses has to be replaced according to Eq. (14) by $\nu_1 = \nu_4 = x$ and $\nu_2 = \nu_3 = y$.

For the derivation of Eqs. (D1)–(D4), we assumed the system to be initially in the ground state $\rho_0(t_1') = \rho(t_0) = |g\rangle\langle g|$, as well as no overlap of the pulses, which allowed us to extend the integration boundaries to $\pm\infty$ in Eq. (25).

IV. DISCUSSION AND RESULTS

We now present how nonsecular conversion processes between the bright and dark state manifolds for the example system can be observed in 2D spectra. A controlled excitation of each manifold is achieved by interaction with either electric fields or field gradients. They can be generated through switching the polarization direction of the incoming light pulse interacting with the plasmonic dolmen structure. The chosen pulse sequence creates coherences between the two excited-state manifolds. Nonsecular processes convert the coherences into excited-state populations. After the pulse sequence, secular processes are filtered out by solely measuring the excited-state populations with PEEM. With the help of the four pathways, Eqs. (D1)–(D4), we compute the electron density n_e measured in PEEM, Eq. (27). Through Fourier transform with respect to the two delay times τ_1 and τ_3,

$$n_e(\tau_4,\Omega_3,\tau_2,\Omega_1) = \int_{-\infty}^{\infty} d\tau_3 d\tau_1\, n_e(\tau_4,\tau_3,\tau_2,\tau_1) e^{-i\Omega_3\tau_3 - i\Omega_1\tau_1}, \tag{28}$$

we obtain a two-dimensional spectrum. It shows on the Ω_1 axis the excited-state coherences during the delay time τ_1, and on the Ω_3 axis the coherences during τ_3, respectively. Before we compare the 2D spectra for our setup with and without secular approximation, we discuss an idealized case of switching between dipole and quadrupole excitation. The concept of the detection protocol can be illustrated most intuitively in the case of ideal switching.

A. Ideal switching

We assume a switching quality of $\eta_x = \eta_y^{-1} = \infty$, opposed to the finite values obtained in the simulation of the plasmonic dolmen structure, Eq. (15). Hence we have $Q_{mn} : \nabla^S \boldsymbol{E}_{\boldsymbol{r}}^x = \boldsymbol{\mu}_{mn} \cdot \boldsymbol{E}_{\boldsymbol{r}}^y = 0$, so that the transition element for x-polarized light is given by a pure dipole coupling $\tilde{\mathcal{M}}_{mn}^x = \boldsymbol{\mu}_{mn} \cdot \boldsymbol{E}_{\boldsymbol{r}}^x$, and for y-polarized light by a pure quadrupole coupling $\tilde{\mathcal{M}}_{mn}^y = Q_{mn} : \nabla^S \boldsymbol{E}_{\boldsymbol{r}}^y$. The chosen pulse sequence [Eq. (14) and Fig. 2] yields only a signal when nonsecular processes are present. Thus in the ideal case we expect the signal to vanish in secular approximation. This can be best explained through Feynman diagrams. In the following, we discuss one process occurring in pathway III and visualize it in the secular and nonsecular case in Fig. 7.

As is illustrated by Eq. (21), in the secular approximation only diagonal elements of the density matrix are coupled to each other. Nondiagonal states, the coherences, solely dephase with time. However, in Fig. 7(a), only coherences are created. Since the bright and dark coherences cannot be converted into populations or other coherences in the secular approximation, the stimulated emission of bright states induced by the fourth pulse is forbidden by selection rules. Therefore the pathway is zero. A similar analysis can be carried out for all possible processes contributing to the diagrams in Fig. 6, leading to an overall vanishing signal in the secular approximation.

Considering the same scattering process including nonsecular terms, conversion between coherences through exciton-

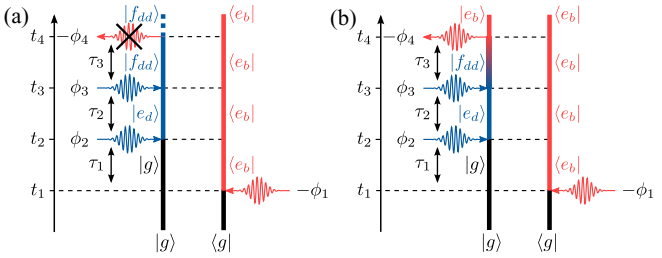

FIG. 7. (Color online) Feynman diagram for pathway III (a) in secular approximation and (b) including nonsecular dynamics. The labeling of the states corresponds to the formation of peak A in the 2D spectra (Figs. 8 and 9). Conversion between states in the secular approximation (a) is restricted to population relaxation, prohibiting the stimulated emission at t_4 and leading to a vanishing signal in PEEM. In (b), nonsecular conversion from $\rho_{f_{dd}e_b} \rightarrow \rho_{f_{bb}e_b}$ during τ_3 produces a measurable signal (indicated by a color gradient from dark blue to light red during τ_3).

phonon processes becomes possible. In Fig. 7(b), a potential process is the conversion between $\rho_{f_{dd}e_b}$ and $\rho_{f_{bb}e_b}$ during τ_3. The system eventually reaches an exciton population, which will generate a signal in PEEM. The peak positions in the 2D spectrum give insight into the particular nonsecular scattering processes occurring within the nanostructure.

In the following, we will discuss the nonsecular 2D spectrum for the model system in the ideal switching case in order to draw conclusions about the involved processes. In Fig. 8, the 2D spectrum $|n_e(0,\Omega_3,\tau_2,\Omega_1)|$ for two delay times $\tau_2 = 72$ fs and $\tau_2 = 94$ fs is shown. On both energy axes, the energies $\omega_{mn} = \omega_m - \omega_n$ of the involved coherences are also indicated. The scale of the plots is adjusted by the function $\mathcal{F}(x) = \text{arcsinh}(x/x_0)$ to highlight small and large features equally [49].

There are two prominent features (peaks A and B) visible in the spectra, both located at the excitation energy of the bright state ω_{ge_b} on the Ω_1 axis (caused by the first pulse in the pulse sequence, which excites a bright state coherence oscillating with the respective energy).

The location of peak A on the Ω_3 axis corresponds to the coherence $\rho_{f_{dd}e_b}$ as indicated in Fig. 8. It is generated by the ESA pathways III and IV at time t_3 (after the third pulse).

The interpretation of peak B is more involved. Three coherences are contributing to this peak: two biexciton-exciton coherences $\rho_{f_{bb}e_b}$ and $\rho_{f_{bd}e_d}$, as well as an exciton-ground state coherence ρ_{e_bg} (compare Fig. 8). All three peaks are located within the exciton linewidth, so that they can only be distinguished indirectly through interference. The excitonic coherence will destructively interfere with the biexcitonic coherences due to an opposite sign between pathways IV and I–III. The oscillatory behavior of this interference can be seen by comparing Figs. 8(a) and (b).

In contrast to peak A at $\omega_{f_{dd}e_b}$, whose corresponding coherence is created by the pulse at t_3 and requires nonsecular conversion after t_3, peak B is the outcome of nonsecular conversion at times before interaction with the pulse at t_4. The excitonic contribution to peak B can be attributed to coherent conversion between $\rho_{e_de_b}$ and $\rho_{e_be_d}$ during the delay time τ_2 in pathway II. The biexcitonic contributions to peak B are a result of conversion processes between $\rho_{f_{dd}e_b}$ and $\rho_{f_{bb}e_b}$, and between $\rho_{f_{dd}e_b}$ and $\rho_{f_{bd}e_d}$ during the delay time τ_3. Unfortunately, a distinction between both biexcitonic processes is not possible since the individual peaks are not spectrally resolvable. The asymmetric line shape of peak B only suggests that both processes mentioned above play a role.

B. Realistic switching

In the last section, we demonstrated that the detection protocol yields a vanishing spectrum for idealized switching between bright and dark state excitation selection rules in the secular approximation. Thus the only contributions to the idealized spectrum originated from nonsecular processes.

In this section, we use the dipole- and quadrupole-field couplings $\boldsymbol{\mu}_{mn} \cdot \boldsymbol{E}_{\boldsymbol{r}}^{\nu_k}$ and $Q_{mn} : \nabla^S \boldsymbol{E}_{\boldsymbol{r}}^{\nu_k}$ computed for the plasmonic dolmen structure, so that the switching quality is given through Eq. (15). Since the quadrupole-field coupling is now $Q_{mn} : \nabla^S \boldsymbol{E}_{\boldsymbol{r}}^{x} \neq 0$, an x-polarized excitation beam will not only excite bright states, but has also a small probability of exciting dark states. The opposite situation will occur for a y-polarized beam since $\boldsymbol{\mu}_{mn} \cdot \boldsymbol{E}_{\boldsymbol{r}}^{y} \neq 0$. As a result of this deviation from the ideal selection rules, remnants of unwanted secular processes will be present in the spectra.

To analyze the impact of imperfect switching on the detection protocol, we will compare the full spectrum for a delay time $\tau_2 = 72$ fs [Fig. 9(a)] with the ideal spectrum discussed before [Fig. 8(a)]. The comparison already suggests that the additional secular processes in the case of realistic switching do not affect the 2D spectrum considerably. The important peaks A and B, indicating nonsecular conversion processes, are still present. The peak intensity of peak B is slightly reduced through destructive interference with secular processes caused by the nonideal selection rules.

To further quantify the error introduced through these additional secular processes, we look at the spectrum in secular approximation in Fig. 9(b). We remember that in the ideal switching case, this spectrum is identical to zero. Thus in the realistic case, it directly constitutes the error introduced through imperfect switching. We recognize some features at $\Omega_1 = \omega_{ge_d}$ and around $\Omega_3 \approx 2$ eV marginally affecting the full spectrum, Fig. 9(a). Furthermore, a large peak B is present in the secular spectrum, which leads to the slight decrease of the peak intensity in the full spectrum. It can be attributed to the bad switching quality η_y^{-1} in Eq. (15). It opens additional pathways with bright state excitation at times t_2 and t_3 (compare Fig. 6). These pathways will create through secular relaxation a signal at the energies $\Omega_3 = \omega_{e_bg}$, $\omega_{f_{bb}e_b}$, and $\omega_{f_{bd}e_d}$. All these contributions taken together constitute the large peak B in Fig. 9(b).

An important observation is that peak A is not present at all in the secular spectrum, suggesting that this peak is solely an effect of nonsecular conversion and cannot be created through secular processes, even in the case of realistic switching. Peak A is therefore a clear signature of nonsecular processes and a delay-time dependent analysis of this peak will thus give insight solely into these processes.

One should keep in mind that the spectra are shown on a nonlinear scale. The amplitude of peak B in the secular spectrum is more than one order of magnitude smaller than the

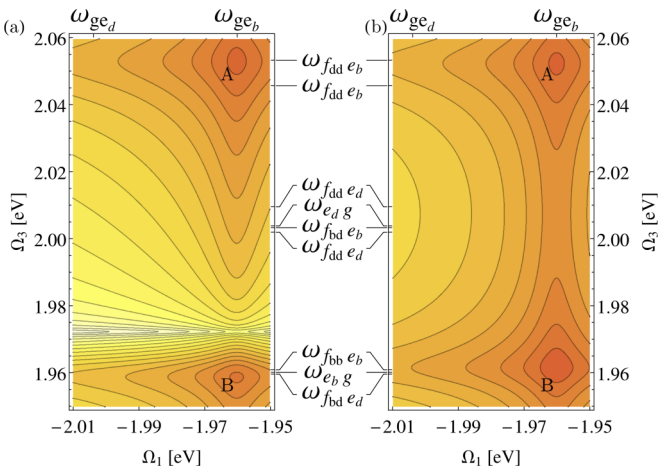

FIG. 8. (Color online) 2D spectra $|n_e(0,\Omega_3,\tau_2,\Omega_1)|$ including nonsecular terms in the ideal case of $Q_{mn}:\nabla^S \boldsymbol{E}_r^x = \boldsymbol{\mu}_{mn}\cdot\boldsymbol{E}_r^y = 0$ for (a) $\tau_2 = 72$ fs and (b) $\tau_2 = 94$ fs. Two distinct features A and B are visible. Destructive interference with the excitonic states leads to a quantum beating behavior. In secular approximation, both spectra vanish.

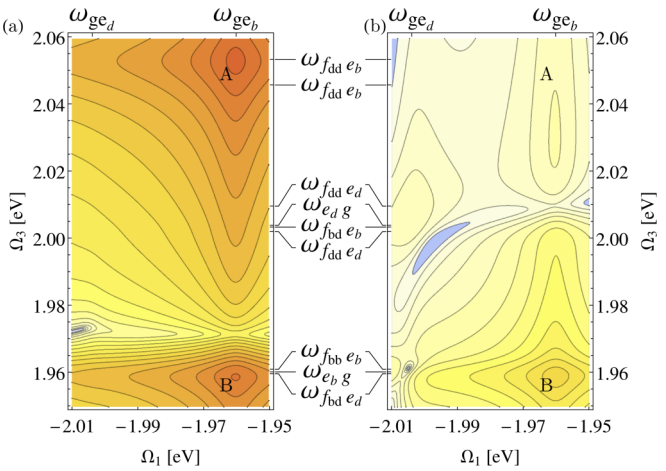

FIG. 9. (Color online) 2D spectrum $|n_e(0,\Omega_3,\tau_2 = 72\text{ fs},\Omega_1)|$ for realistic switching quality η_{ν_k}, Eq. (15) (a) including nonsecular processes and (b) in secular approximation. The realistic switching in (a) introduces only a minor error compared to Fig. 8(a). This error is directly represented through (b).

nonsecular signal, thus we have an error of <10%. For peak A, we have an error of ∼0.1%, since this peak is completely absent in the secular spectrum.

As a final remark, the limitation of this detection protocol should also be pointed out. We applied this protocol to detect nonsecular conversion processes between the bright and dark state manifolds, though it is not possible to detect nonsecular conversion within each manifold since there always have to be at least two selectively excitable manifolds of states present in the system. However, the protocol can be extended to detection between other manifolds, e.g., through spin-sensitive excitation.

V. CONCLUSION

In this paper, we presented the theoretical outline for a detection protocol of nonsecular conversion processes. We derived the signal generated by the protocol from the fourth-order density matrix response to four ultrashort light pulses. The detection protocol is sensitive to nonsecular processes between different subsets of transitions. Here, we used the subsets of dipole-allowed and dipole-forbidden transitions, though this protocol can be extended to arbitrary subsets (for example spin-up and spin-down excitation in semiconductors through circularly polarized light). To access dipole-forbidden excitations, we expanded the light-matter interaction by inclusion of field-gradient interactions. We presented a possible way of switching between excitation of dipole-allowed and dipole-forbidden transitions through a plasmonic dolmen structure.

The protocol was applied to a CdSe QD in a ZnS NR. Even for the simple relaxation treatment in Born-Markov approximation, we were able to extract the small signal generated through nonsecular processes out of the large contribution of secular processes. The experimental realization using similar protocols, for example on semiconductor systems and biological photosynthetic or synthetic dyes, could lead to direct investigation of non-Markovian effects.

ACKNOWLEDGMENTS

We thank A. Knorr for insightful discussion and acknowledge support from the Deutsche Forschungsgemeinschaft (DFG) through the priority program SPP 1391 (Ultrafast Nanooptics).

APPENDIX A: UNPERTURBED SYSTEM

The electronic Hamiltonian is derived under the assumption of the envelope approximation for the electronic wave functions, Eq. (5), and includes the Coulomb interaction of electrons and holes:

$$H_0 = \sum_i \varepsilon_{i,c} e_i^\dagger e_i - \sum_j \varepsilon_{j,v} h_j^\dagger h_j - \sum_{ij} V_{ji}^{ij} e_i^\dagger h_j^\dagger h_j e_i + \frac{1}{2}\sum_{ij} V_{ji}^{ij} e_i^\dagger e_j^\dagger e_j e_i + \frac{1}{2}\sum_{ij} V_{ji}^{ij} h_i^\dagger h_j^\dagger h_j h_i. \quad \text{(A1)}$$

The last two terms introduce the biexcitonic shifts. The Coulomb integrals are given by

$$V_{kl}^{ij} = \frac{e^2}{4\pi\varepsilon_0\varepsilon}\delta_{\lambda_i\lambda_l}\delta_{\lambda_j\lambda_k}\delta_{\sigma_i\sigma_l}\delta_{\sigma_j\sigma_k}\int d\boldsymbol{r}d\boldsymbol{r}'\,\varphi_{i,\lambda_i}^*(\boldsymbol{r})\varphi_{j,\lambda_j}^*(\boldsymbol{r}') \times \frac{1}{|\boldsymbol{r}-\boldsymbol{r}'|}\varphi_{k,\lambda_k}(\boldsymbol{r}')\varphi_{l,\lambda_l}(\boldsymbol{r}), \quad \text{(A2)}$$

where we only consider monopole-monopole corrections to the interaction-free Hamiltonian. Thus the Hamiltonian remains diagonal after inclusion of the Coulomb terms. The Coulomb elements possess the symmetry $V_{kl}^{ij} = V_{lk}^{ji} = V_{ij}^{kl*} = V_{ji}^{lk*}$.

We introduce the excitonic states

$$|e_m\rangle = e_i^\dagger h_j^\dagger |g\rangle \quad \text{(A3)}$$

with the multi-index $e_m = \{i,j\}$ labeling the excitonic state m with electron in state i and hole in state j. Analogously, the biexcitonic state is

$$|f_m\rangle = e_i^\dagger e_j^\dagger h_k^\dagger h_l^\dagger |g\rangle \tag{A4}$$

with the multi-index $f_m = \{ij,kl\}$ for electrons in state i and j, as well as holes in states k and l. The Hamiltonian can be reformulated as

$$H_0 = \sum_{e_m} \varepsilon_{e_m} |e_m\rangle\langle e_m| + \sum_{f_m} \varepsilon_{f_m} |f_m\rangle\langle f_m|, \tag{A5}$$

with the energies

$$\begin{aligned} \varepsilon_{e_m} &= \varepsilon_{i,c} - \varepsilon_{j,v} - V_{ji}^{ij}, \\ \varepsilon_{f_m} &= \varepsilon_{i,c} + \varepsilon_{j,c} - \varepsilon_{k,v} - \varepsilon_{l,v} \\ &\quad -\left(V_{ki}^{ik} + V_{li}^{il} + V_{kj}^{jk} + V_{lj}^{jl}\right) + \left(V_{ji}^{ij} + V_{lk}^{kl}\right). \end{aligned} \tag{A6}$$

We further reduce the notation by collecting both excitonic and biexcitonic states into a generic index m:

$$H_0 = \sum_m \varepsilon_m |m\rangle\langle m|. \tag{A7}$$

APPENDIX B: HIGHER-ORDER EXCITON-LIGHT INTERACTION

We start from a semiclassical interaction between electrons and electric fields derived in Ref. [81] in its second quantized form (for simplicity $\boldsymbol{r}_0 = 0$):

$$H_{e\text{-}L} = -e \int d\boldsymbol{r}\, \psi^\dagger(\boldsymbol{r}) \left[\boldsymbol{r} \cdot \boldsymbol{E}(0,t) + \frac{1}{2} \boldsymbol{r} \circ \boldsymbol{r} : \nabla \boldsymbol{E}(0,t) \right] \psi(\boldsymbol{r}). \tag{B1}$$

The first term is the dipole interaction, and the second term is the quadrupole interaction. We use the envelope approximation, Eq. (5) and transform into electron-hole picture. Additional separation of length scales $\boldsymbol{r} \to \boldsymbol{r}_n + \boldsymbol{r}'$ (where $\boldsymbol{r}_n$ is pointing to unit cell n and $\boldsymbol{r}'$ varies within the unit cell) leads to

$$\begin{aligned} H_{e-L} = -e \sum_{ij} \sum_{\boldsymbol{r}_n} \int_{UC} d\boldsymbol{r}' \Big[& (\boldsymbol{r}_n + \boldsymbol{r}') \cdot \boldsymbol{E}(0,t) \\ & + \frac{1}{2} (\boldsymbol{r}_n + \boldsymbol{r}') \circ (\boldsymbol{r}_n + \boldsymbol{r}') : \nabla \boldsymbol{E}(0,t) \Big] \\ & \times \left[\varphi_{i,c}^*(\boldsymbol{r}_n) \varphi_{j,v}(\boldsymbol{r}_n) u_c^{\sigma_i *}(\boldsymbol{r}') u_v^{\sigma_j}(\boldsymbol{r}') e_i^\dagger h_j^\dagger + \text{H.a.} \right], \end{aligned} \tag{B2}$$

where we only considered interband transitions.

In principle, magnetic dipole interactions have to be included in the discussion as well. However, the magnetic fields at $\boldsymbol{r}_0$ are weak and will therefore be neglected in the discussion (checked in microscopic calculations, not included in the paper).

1. Dipole interaction

We take the first term of Eq. (B2) with the constant electric field and convert the sum over $\boldsymbol{r}_n$ into an integral. As done in Appendix A, we introduce excitonic states $|e_m\rangle$ with the multi-index $e_m = \{i,j\}$. We define the microscopic dipole element,

$$\boldsymbol{d}_{cv}^{\sigma_m} = \boldsymbol{d}_{vc}^{\sigma_m *} = \int_{UC} d\boldsymbol{r}'\, u_c^{\sigma_m *}(\boldsymbol{r}')\, \boldsymbol{r}'\, u_v^{\sigma_m}(\boldsymbol{r}') \delta_{\sigma_m \sigma_n}, \tag{B3}$$

which provides information about the directional character of light absorption depending on the crystal structure and orientation, and the overlap integral between the envelope wave functions

$$S_{e_m g} = \int d\boldsymbol{r}\, \varphi_{e_m,c}^*(\boldsymbol{r}) \varphi_{e_m,v}(\boldsymbol{r}). \tag{B4}$$

Thus, we can write the dipole contribution to the light-matter interaction for excitons:

$$H_{e\text{-}L}^{(0)}\big|_{\text{ex}} = -e \sum_{e_m} \left[\boldsymbol{d}_{cv}^{\sigma_{e_m}} S_{e_m g} |e_m\rangle\langle g| + \text{H.a.} \right] \cdot \boldsymbol{E}(0,t). \tag{B5}$$

We proceed analogously with biexcitons according to above notation,

$$H_{e\text{-}L}^{(0)}\big|_{\text{biex}} = -e \sum_{f_m e_n} \left[\boldsymbol{d}_{cv}^{\sigma_{e_m}} S_{f_m e_n} |f_m\rangle\langle e_n| + \text{H.a.} \right] \cdot \boldsymbol{E}(0,t). \tag{B6}$$

We apply the factorization of the electric field, Eq. (7). Again, we combine both Hamiltonians, Eqs. (B5) and (B6), to condense the notation:

$$H_{e\text{-}L}^{(0)} = -\sum_k \sum_{\substack{mn \\ \text{intraband}}} \boldsymbol{\mu}_{mn} \cdot \boldsymbol{E}_{\boldsymbol{r}}^{\nu_k} E_t^k(t - t_k) |m\rangle\langle n|. \tag{B7}$$

The dipole-field coupling is given by

$$\boldsymbol{\mu}_{mn} = e\, S_{mn} \boldsymbol{d}_{cv}^{\sigma_m}. \tag{B8}$$

2. Quadrupole interaction

We turn back to Eq. (B2) and collect all terms with electric-field gradients. To simplify the expression, we note that the integral $\int d\boldsymbol{r}'\, u_c^{\sigma_m *}(\boldsymbol{r}') u_v^{\sigma_m}(\boldsymbol{r}')$ vanishes, since Bloch-functions of different bands are orthogonal. The integral $\int d\boldsymbol{r}'\, u_c^{\sigma_m *}(\boldsymbol{r}')\, \boldsymbol{r}' \circ \boldsymbol{r}'\, u_v^{\sigma_m}(\boldsymbol{r}')$ is assumed to be small and will therefore be neglected.

The remaining terms are treated analogous to the previous section. We introduce the dipole element of the envelope wave function

$$\boldsymbol{m}_{e_m g} = \int d\boldsymbol{r}\, \varphi_{e_m,c}^*(\boldsymbol{r})\, \boldsymbol{r}\, \varphi_{e_m,v}(\boldsymbol{r}), \tag{B9}$$

and the notation $\boldsymbol{a} \cdot A \cdot \boldsymbol{b} = \boldsymbol{b} \cdot A^T \cdot \boldsymbol{a} = \boldsymbol{a} \circ \boldsymbol{b} : A = \boldsymbol{b} \circ \boldsymbol{a} : A^T$ with the dyadic product $\boldsymbol{a} \circ \boldsymbol{b}$ and the Frobenius inner product defined in Eq. (11) [82]. Through $\nabla^S \boldsymbol{E} := 1/2(\nabla \boldsymbol{E} + \nabla \boldsymbol{E}^T)$ we can simplify the expression to

$$H_{e\text{-}L}^{(1)}\big|_{\text{ex}} = -e \sum_{e_m} \left[\left(\boldsymbol{d}_{cv}^{\sigma_{e_m}} \circ \boldsymbol{m}_{e_m g} \right) |e_m\rangle\langle g| + \text{H.a.} \right] : \nabla^S \boldsymbol{E}(0,t). \tag{B10}$$

The biexcitonic contribution can also be derived accordingly. Again, we apply the approximation (7) and collect the excitonic and biexcitonic contribution to obtain

$$H_{e\text{-}L}^{(1)} = -\sum_k \sum_{\substack{mn \\ \text{intraband}}} Q_{mn} : \nabla^S \boldsymbol{E}_{\boldsymbol{r}}^{\nu_k} E_t^k(t - t_k) |m\rangle\langle n| \tag{B11}$$

with

$$Q_{mn} = e\left(\boldsymbol{d}_{cv}^{\sigma_m} \circ \boldsymbol{m}_{mn}\right). \tag{B12}$$

APPENDIX C: PHONON INTERACTION

For the electron-phonon interaction we consider the Hamiltonian for Fröhlich coupling between electrons and optical phonons [109],

$$H_{e\text{-}ph} = e\sum_q \int d\boldsymbol{r}\, \psi^\dagger(\boldsymbol{r})\phi_q(\boldsymbol{r})\psi(\boldsymbol{r}), \tag{C1}$$

which originates from the polarization induced by the electrostatic potential ϕ_q of the phonon-mode q. As done before, we transform the Hamiltonian into the electron-hole picture under assumption of the envelope approximation, Eq. (5). Furthermore, we drop the phonon interaction with the ground state. Thus we get [90]

$$H_{e\text{-}ph} = \hbar\sum_q \left[\sum_{ij}\left(g_{q,c}^{ij} b_q^\dagger + g_{q,c}^{ji*} b_q\right) e_i^\dagger e_j - \sum_{ij}\left(g_{q,v}^{ij} b_q^\dagger + g_{q,v}^{ji*} b_q\right) h_j^\dagger h_i\right] \tag{C2}$$

with the phonon-coupling elements

$$g_{q,\lambda}^{ij} = \frac{e}{4\pi\varepsilon_0\varepsilon\hbar}\int d\boldsymbol{r}\, \varphi_{i,\lambda_i}^*(\boldsymbol{r})\varphi_{j,\lambda_j}(\boldsymbol{r})\phi_q(\boldsymbol{r})\delta_{\lambda_i\lambda_j}\delta_{\sigma_i\sigma_j}. \tag{C3}$$

For the phonon potentials $\phi_q(\boldsymbol{r})$, we consider cylindrical longitudinal optical (LO) and side-surface optical (SSO) phonons of a nanorod as calculated in Ref. [90]. They interact with the spherical electron wave functions in the QD. We assume that the phonons are not influenced by the QD within the rod and that the QD is positioned in the center of the NR. Acoustic phonons were neglected since their energy is too small to surpass the transition energy between the energy levels.

Again, we transform the Hamiltonian into the exciton - picture through Eqs. (A3) and (A4):

$$H_{e\text{-}ph} = \hbar\sum_{q e_m e_n}\left(g_q^{e_m e_n} b_q^\dagger + g_q^{e_n e_m *} b_q\right)|e_m\rangle\langle e_n| + \hbar\sum_{q f_m f_n}\left(g_q^{f_m f_n} b_q^\dagger + g_q^{f_n f_m *} b_q\right)|f_m\rangle\langle f_n|. \tag{C4}$$

The excitonic phonon coupling elements for two excitons $|e_m\rangle = |i,k\rangle, |e_n\rangle = |j,l\rangle$ are

$$g_q^{e_m e_n} = g_{q,c}^{ij}\delta_{kl} - g_{q,v}^{lk}\delta_{ij} \tag{C5}$$

and for two biexcitons $|f_m\rangle = |ij,kl\rangle, |f_n\rangle = |i'j',k'l'\rangle$:

$$\begin{aligned} g_q^{f_m f_n} = {} & \left(g_{q,c}^{ii'}\delta_{jj'} + g_{q,c}^{jj'}\delta_{ii'} - g_{q,c}^{ij'}\delta_{ji'} - g_{q,c}^{ji'}\delta_{ij'}\right) \\ & \times(\delta_{kk'}\delta_{ll'} - \delta_{kl'}\delta_{lk'}) \\ & - \left(g_{q,v}^{k'k}\delta_{ll'} + g_{q,v}^{l'l}\delta_{kk'} - g_{q,v}^{k'l}\delta_{lk'} - g_{q,v}^{l'k}\delta_{kl'}\right) \\ & \times(\delta_{ii'}\delta_{jj'} - \delta_{ij'}\delta_{ji'}). \end{aligned} \tag{C6}$$

The δ_{ij} between the states also implies $\delta_{\sigma_i\sigma_j}$ between their spin degree of freedom.

We introduce the shorthand notation as in the previous sections through

$$H_{e\text{-}ph} = \hbar\sum_q \sum_{\substack{mn \\ \text{intraband}}}\left(g_q^{mn} b_q^\dagger + g_q^{nm*} b_q\right)|m\rangle\langle n|. \tag{C7}$$

APPENDIX D: LIOUVILLE PATHWAYS

Upon evaluation of Eq. (25) with the light-coupling Hamiltonian, Eq. (8), as described in the main text, we get the analytical expressions for all contributing pathways:

$$\rho_{I,e_i e_j}^{(4)}(\tau_4,\tau_3,\tau_2,\tau_1) = -\frac{1}{\hbar^4}\sum_{e_1\ldots e_5}\mathcal{G}_{e_i e_j,e_4 e_5}(\tau_4)\tilde{\mathcal{M}}_{g e_5}^{\nu_4}\mathcal{G}_{e_4 g,e_3 g}(\tau_3)\tilde{\mathcal{M}}_{e_3 g}^{\nu_3}\tilde{\mathcal{M}}_{e_2 g}^{\nu_2}\mathcal{G}_{g e_2,g e_1}(\tau_1)\tilde{\mathcal{M}}_{g e_1}^{\nu_1} \times\tilde{E}_4^*(\omega_4)\tilde{E}_3(\omega_3)\tilde{E}_2(\omega_2)\tilde{E}_1^*(\omega_1)e^{i\phi_s}, \tag{D1}$$

$$\rho_{II,e_i e_j}^{(4)}(\tau_4,\tau_3,\tau_2,\tau_1) = -\frac{1}{\hbar^4}\sum_{e_1\ldots e_7}\mathcal{G}_{e_i e_j,e_6 e_7}(\tau_4)\tilde{\mathcal{M}}_{g e_7}^{\nu_4}\mathcal{G}_{e_6 g,e_5 g}(\tau_3)\tilde{\mathcal{M}}_{e_4 g}^{\nu_3}\mathcal{G}_{e_5 e_4,e_3 e_2}(\tau_2)\tilde{\mathcal{M}}_{e_3 g}^{\nu_2}\mathcal{G}_{g e_2,g e_1}(\tau_1)\tilde{\mathcal{M}}_{g e_1}^{\nu_1} \times\tilde{E}_4^*(\omega_4)\tilde{E}_3(\omega_3)\tilde{E}_2(\omega_2)\tilde{E}_1^*(\omega_1)e^{i\phi_s}, \tag{D2}$$

$$\rho_{III,e_i e_j}^{(4)}(\tau_4,\tau_3,\tau_2,\tau_1) = -\frac{1}{\hbar^4}\sum_{e_1\ldots e_7}\sum_{f_1,f_2}\mathcal{G}_{e_i e_j,e_7 e_6}(\tau_4)\tilde{\mathcal{M}}_{e_7 f_2}^{\nu_4}\mathcal{G}_{f_2 e_6,f_1 e_4}(\tau_3)\tilde{\mathcal{M}}_{f_1 e_5}^{\nu_3}\mathcal{G}_{e_5 e_4,e_3 e_2}(\tau_2)\tilde{\mathcal{M}}_{e_3 g}^{\nu_2}\mathcal{G}_{g e_2,g e_1}(\tau_1)\tilde{\mathcal{M}}_{g e_1}^{\nu_1} \times\tilde{E}_4^*(\omega_4)\tilde{E}_3(\omega_3)\tilde{E}_2(\omega_2)\tilde{E}_1^*(\omega_1)e^{i\phi_s}, \tag{D3}$$

$$\rho_{IV,f_i f_j}^{(4)}(\tau_4,\tau_3,\tau_2,\tau_1) = +\frac{1}{\hbar^4}\sum_{e_1\ldots e_6}\sum_{f_1\ldots f_3}\mathcal{G}_{f_i f_j,f_2 f_3}(\tau_4)\tilde{\mathcal{M}}_{e_6 f_3}^{\nu_4}\mathcal{G}_{f_2 e_6,f_1 e_4}(\tau_3)\tilde{\mathcal{M}}_{f_1 e_5}^{\nu_3}\mathcal{G}_{e_5 e_4,e_3 e_2}(\tau_2)\tilde{\mathcal{M}}_{e_3 g}^{\nu_2}\mathcal{G}_{g e_2,g e_1}(\tau_1)\tilde{\mathcal{M}}_{g e_1}^{\nu_1} \times\tilde{E}_4^*(\omega_4)\tilde{E}_3(\omega_3)\tilde{E}_2(\omega_2)\tilde{E}_1^*(\omega_1)e^{i\phi_s}. \tag{D4}$$

They correspond to the Feynman diagrams in Fig. 6.

[1] H. Breuer and F. Petruccione, *The Theory of Open Quantum Systems* (Oxford University Press, New York, 2002).
[2] S. Mukamel, Chem. Phys. **37**, 33 (1979).
[3] S. Mukamel, I. Oppenheim, and J. Ross, Phys. Rev. A **17**, 1988 (1978).
[4] R. Kubo, J. Math. Phys. **4**, 174 (1963).
[5] J. H. Freed, J. Chem. Phys. **49**, 376 (1968).
[6] S. Nakajima, Prog. Theor. Phys. **20**, 948 (1958).
[7] R. Zwanzig, J. Chem. Phys. **33**, 1338 (1960).
[8] N. Hashitsumae, F. Shibata, and M. Shingū, J. Stat. Phys. **17**, 155 (1977).
[9] S. Chaturvedi and F. Shibata, Z. Phys. B **35**, 297 (1979).
[10] F. Shibata, Y. Takahashi, and N. Hashitsume, J. Stat. Phys. **17**, 171 (1977).
[11] M. Richter and A. Knorr, Ann. Phys. **325**, 711 (2010).
[12] Y. Tanimura and R. Kubo, J. Phys. Soc. Jpn. **58**, 101 (1989).
[13] Y. Tanimura, Phys. Rev. A **41**, 6676 (1990).
[14] H. Haug, Phys. Status Solidi B **173**, 139 (1992).
[15] L. Bányai, D. B. T. Thoai, C. Remling, and H. Haug, Phys. Status Solidi B **173**, 149 (1992).
[16] A. Ishizaki and Y. Tanimura, Chem. Phys. **347**, 185 (2008).
[17] G. Schaller, P. Zedler, and T. Brandes, Phys. Rev. A **79**, 032110 (2009).
[18] C. Fleming, N. I. Cummings, C. Anastopoulos, and B. L. Hu, J. Phys. A **43**, 405304 (2010).
[19] G. S. Agarwal, Phys. Rev. A **7**, 1195 (1973).
[20] P. Haikka and S. Maniscalco, Phys. Rev. A **81**, 052103 (2010).
[21] H. Mäkelä and M. Möttönen, Phys. Rev. A **88**, 052111 (2013).
[22] T.-C. Dinh and T. Renger, J. Chem. Phys. **142**, 034104 (2015).
[23] J. P. Pekola, V. Brosco, M. Möttönen, P. Solinas, and A. Shnirman, Phys. Rev. Lett. **105**, 030401 (2010).
[24] P. Solinas, M. Möttönen, J. Salmilehto, and J. P. Pekola, Phys. Rev. B **82**, 134517 (2010).
[25] P. Solinas, M. Möttönen, J. Salmilehto, and J. P. Pekola, Phys. Rev. B **85**, 024527 (2012).
[26] J. Jeske, D. J. Ing, M. B. Plenio, S. F. Huelga, and J. H. Cole, J. Chem. Phys. **142**, 064104 (2015).
[27] G. Schaller, G. Kießlich, and T. Brandes, Phys. Rev. B **80**, 245107 (2009).
[28] P. Karwat and P. Machnikowski, Phys. Rev. B **91**, 125428 (2015).
[29] F. Intravaia, S. Maniscalco, and A. Messina, Eur. Phys. J. B **32**, 97 (2003).
[30] J. Salmilehto, P. Solinas, and M. Möttönen, Phys. Rev. A **85**, 032110 (2012).
[31] A. Redfield, IBM J. Res. Dev. **1**, 19 (1957).
[32] A. Redfield, in *Advances in Magnetic Resonance*, Advances in Magnetic and Optical Resonance Vol. 1, edited by J. S. Waugh (Academic, New York, 1965), pp. 1–32.
[33] K. Blum, *Density Matrix Theory and Applications*, Physics of Atoms and Molecules (Springer, New York, 1996).
[34] Y. Tanimura and S. Mukamel, J. Chem. Phys. **99**, 9496 (1993).
[35] K. Okumura and Y. Tanimura, J. Chem. Phys. **107**, 2267 (1997).
[36] A. Tokmakoff, M. J. Lang, D. S. Larsen, G. R. Fleming, V. Chernyak, and S. Mukamel, Phys. Rev. Lett. **79**, 2702 (1997).
[37] J. Bredenbeck, J. Helbing, C. Kolano, and P. Hamm, ChemPhysChem **8**, 1747 (2007).
[38] W. P. Aue, E. Bartholdi, and R. R. Ernst, J. Chem. Phys. **64**, 2229 (1976).
[39] S. Mukamel, Annu. Rev. Phys. Chem. **51**, 691 (2000).
[40] D. Abramavicius, B. Palmieri, D. V. Voronine, F. Šanda, and S. Mukamel, Chem. Rev. **109**, 2350 (2009).
[41] M. Cho, Chem. Rev. **108**, 1331 (2008).
[42] D. M. Jonas, Annu. Rev. Phys. Chem. **54**, 425 (2003).
[43] S. Mukamel, *Principles of Nonlinear Optical Spectroscopy*, Oxford series in optical and imaging sciences (Oxford University Press, New York, 1995).
[44] M. Cowan, J. Ogilvie, and R. Miller, Chem. Phys. Lett. **386**, 184 (2004).
[45] M. Cho, H. M. Vaswani, T. Brixner, J. Stenger, and G. R. Fleming, J. Phys. Chem. B **109**, 10542 (2005).
[46] A. V. Pisliakov, T. Mančal, and G. R. Fleming, J. Chem. Phys. **124**, 234505 (2006).
[47] T. Zhang, I. Kuznetsova, T. Meier, X. Li, R. P. Mirin, P. Thomas, and S. T. Cundiff, Proc. Natl. Acad. Sci. USA **104**, 14227 (2007).
[48] Y.-C. Cheng, G. S. Engel, and G. R. Fleming, Chem. Phys. **341**, 285 (2007).
[49] B. P. Fingerhut, M. Richter, J.-W. Luo, A. Zunger, and S. Mukamel, Ann. Phys. **525**, 31 (2013).
[50] S. Mukamel and M. Richter, Phys. Rev. A **83**, 013815 (2011).
[51] M. Krecik, S. M. Hein, M. Schoth, and M. Richter, Proc. SPIE **9361**, 936109 (2015).
[52] B. P. Fingerhut, M. Richter, J.-W. Luo, A. Zunger, and S. Mukamel, Phys. Rev. B **86**, 235303 (2012).
[53] K. W. Stone, K. Gundogdu, D. B. Turner, X. Li, S. T. Cundiff, and K. A. Nelson, Science **324**, 1169 (2009).
[54] M. Richter, F. Schlosser, M. Schoth, S. Burger, F. Schmidt, A. Knorr, and S. Mukamel, Phys. Rev. B **86**, 085308 (2012).
[55] F. Schlosser, A. Knorr, S. Mukamel, and M. Richter, New J. Phys. **15**, 025004 (2013).
[56] F. Schlosser, M. Schoth, K. Hiremath, S. Burger, F. Schmidt, A. Knorr, S. Mukamel, and M. Richter, Proc. SPIE **8260**, 82601V (2012).
[57] J. R. Caram, H. Zheng, P. D. Dahlberg, B. S. Rolczynski, G. B. Griffin, D. S. Dolzhnikov, D. V. Talapin, and G. S. Engel, J. Chem. Phys. **140**, 084701 (2014).
[58] X. Li, T. Zhang, C. N. Borca, and S. T. Cundiff, Phys. Rev. Lett. **96**, 057406 (2006).
[59] G. S. Engel, T. R. Calhoun, E. L. Read, T.-K. Ahn, T. Mančal, Y.-C. Cheng, R. E. Blankenship, and G. R. Fleming, Nature (London) **446**, 782 (2007).
[60] W. M. Zhang, T. Meier, V. Chernyak, and S. Mukamel, J. Chem. Phys. **108**, 7763 (1998).
[61] G. Panitchayangkoon, D. V. Voronine, D. Abramavicius, J. R. Caram, N. H. C. Lewis, S. Mukamel, and G. S. Engel, Proc. Natl. Acad. Sci. USA **108**, 20908 (2011).
[62] T. Brixner, J. Stenger, H. M. Vaswani, M. Cho, R. E. Blankenship, and G. R. Fleming, Nature (London) **434**, 625 (2005).
[63] T. Brixner, T. Mančal, I. V. Stiopkin, and G. R. Fleming, J. Chem. Phys. **121**, 4221 (2004).
[64] F. Caycedo-Soler, A. W. Chin, J. Almeida, S. F. Huelga, and M. B. Plenio, J. Chem. Phys. **136**, 155102 (2012).
[65] B. Hein, C. Kreisbeck, T. Kramer, and M. Rodríguez, New J. Phys. **14**, 023018 (2012).

[66] C. Kreisbeck, T. Kramer, and A. Aspuru-Guzik, J. Phys. Chem. B **117**, 9380 (2013).

[67] M. Aeschlimann, T. Brixner, A. Fischer, C. Kramer, P. Melchior, W. Pfeiffer, C. Schneider, C. Strüber, P. Tuchscherer, and D. V. Voronine, Science **333**, 1723 (2011).

[68] M. Aeschlimann, M. Bauer, D. Bayer, T. Brixner, S. Cunovic, F. Dimler, A. Fischer, W. Pfeiffer, M. Rohmer, C. Schneider, F. Steeb, C. Strüber, and D. V. Voronine, Proc. Natl. Acad. Sci. USA **107**, 5329 (2010).

[69] M. Aeschlimann, M. Bauer, D. Bayer, T. Brixner, F. J. G. de Abajo, W. Pfeiffer, M. Rohmer, C. Spindler, and F. Steeb, Nature (London) **446**, 301 (2007).

[70] T. Brixner, F. J. García de Abajo, J. Schneider, and W. Pfeiffer, Phys. Rev. Lett. **95**, 093901 (2005).

[71] O. Schmidt, M. Bauer, C. Wiemann, R. Porath, M. Scharte, O. Andreyev, G. Schönhense, and M. Aeschlimann, Appl. Phys. B **74**, 223 (2002).

[72] M. I. Stockman, Opt. Express **19**, 22029 (2011).

[73] M. I. Stockman, Phys. Today **64**(2), 39 (2011).

[74] V. Giannini, A. I. Fernández-Domínguez, Y. Sonnefraud, T. Roschuk, R. Fernández-García, and S. A. Maier, Small **6**, 2498 (2010).

[75] C. Ropers, C. C. Neacsu, T. Elsaesser, M. Albrecht, M. B. Raschke, and C. Lienau, Nano Lett. **7**, 2784 (2007).

[76] P. Mühlschlegel, H.-J. Eisler, O. J. F. Martin, B. Hecht, and D. W. Pohl, Science **308**, 1607 (2005).

[77] M. Fu, K. Wang, H. Long, G. Yang, P. Lu, F. Hetsch, A. S. Susha, and A. L. Rogach, Appl. Phys. Lett. **100**, 063117 (2012).

[78] E. Cohen-Hoshen, G. W. Bryant, I. Pinkas, J. Sperling, and I. Bar-Joseph, Nano Lett. **12**, 4260 (2012).

[79] A. Ridolfo, O. Di Stefano, N. Fina, R. Saija, and S. Savasta, Phys. Rev. Lett. **105**, 263601 (2010).

[80] S. M. Hein and H. Giessen, Phys. Rev. Lett. **111**, 026803 (2013).

[81] L. D. Barron and C. G. Gray, J. Phys. A **6**, 59 (1973).

[82] R. Horn and C. Johnson, *Matrix Analysis* (Cambridge University Press, Cambridge, UK, 2012).

[83] B. Luk'yanchuk, N. I. Zheludev, S. A. Maier, N. J. Halas, P. Nordlander, H. Giessen, and C. T. Chong, Nat. Mater. **9**, 707 (2010).

[84] B. Gallinet and O. J. F. Martin, ACS Nano **5**, 8999 (2011).

[85] V. Giannini, Y. Francescato, H. Amrania, C. C. Phillips, and S. A. Maier, Nano Lett. **11**, 2835 (2011).

[86] N. Verellen, Y. Sonnefraud, H. Sobhani, F. Hao, V. V. Moshchalkov, P. V. Dorpe, P. Nordlander, and S. A. Maier, Nano Lett. **9**, 1663 (2009).

[87] V. Grigoriev, S. Varault, G. Boudarham, B. Stout, J. Wenger, and N. Bonod, Phys. Rev. A **88**, 063805 (2013).

[88] M. Kasperczyk, S. Person, D. Ananias, L. D. Carlos, and L. Novotny, Phys. Rev. Lett. **114**, 163903 (2015).

[89] G. F. Quinteiro and T. Kuhn, Phys. Rev. B **90**, 115401 (2014).

[90] W.-S. Li and C.-Y. Chen, Phys. B (Amsterdam, Neth.) **229**, 375 (1997).

[91] L. Berger, *Semiconductor Materials* (Taylor & Francis, London, 1996).

[92] W. W. Piper, D. T. F. Marple, and P. D. Johnson, Phys. Rev. **110**, 323 (1958).

[93] S.-H. Wei and A. Zunger, Appl. Phys. Lett. **72**, 2011 (1998).

[94] R. Chen, D. L. Lin, and T. F. George, Phys. Rev. B **41**, 1435 (1990).

[95] H. Haug and S. Koch, *Quantum Theory of the Optical and Electronic Properties of Semiconductors* (World Scientific, Singapore, 2009).

[96] L. Novotny and B. Hecht, *Principles of Nano-Optics*, (Cambridge University Press, Cambridge, UK, 2012).

[97] B. Willingham, D. Brandl, and P. Nordlander, Appl. Phys. B **93**, 209 (2008).

[98] A. M. Funston, C. Novo, T. J. Davis, and P. Mulvaney, Nano Lett. **9**, 1651 (2009).

[99] C.-Y. Tsai, J.-W. Lin, C.-Y. Wu, P.-T. Lin, T.-W. Lu, and P.-T. Lee, Nano Lett. **12**, 1648 (2012).

[100] A. E. Miroshnichenko, S. Flach, and Y. S. Kivshar, Rev. Mod. Phys. **82**, 2257 (2010).

[101] L. Chuntonov and G. Haran, Nano Lett. **11**, 2440 (2011).

[102] G. D. Scholes, J. Chem. Phys. **121**, 10104 (2004).

[103] G. D. Scholes and D. L. Andrews, Phys. Rev. B **72**, 125331 (2005).

[104] COMSOL MULTIPHYSICS 4.4.

[105] T. Takagahara, Phys. Rev. Lett. **71**, 3577 (1993).

[106] A naive application of the secular approximation only demands a degeneracy between the states. However, for near-degenerate levels, this would nevertheless lead to a breakdown of the approximation due to slow-oscillating coherences [18,26].

[107] R. P. Feynman, Phys. Rev. **84**, 108 (1951).

[108] P. Tian, D. Keusters, Y. Suzaki, and W. S. Warren, Science **300**, 1553 (2003).

[109] T. Takagahara, Phys. Rev. B **47**, 4569 (1993).